# Supporting Information

# Regulating the Crystalline Structure and Ion Affinity of Covalent Organic Frameworks for Enhanced Lithium/Magnesium Separation

*Chuncai Wang[1,2], Shiwen Bao[1,2], Yanfeng Gong[1,2], Lei Yu[1,2], Zizhe Xu[1], Chul. B Park[1], Kunyan Sui[1], Jun Gao[2,3,]*, and Xueli Liu[1,]**

[1]College of Materials Science and Engineering, Key Laboratory of Marine Bio-based Fibers of Shandong Province, Key Laboratory of Shandong Provincial Universities for Advanced Fibers and Composites, Qingdao University, Qingdao 266071, China

[2]Qingdao Institute of Bioenergy and Bioprocess Technology, Chinese Academy of Sciences, Qingdao 266101, China

[3] Shandong Energy Institute, Qingdao 266101, China

*Corresponding author

Email**:** jun.gao@qibebt.ac.cn (J. Gao); liuxl@qdu.edu.cn (X. Liu)

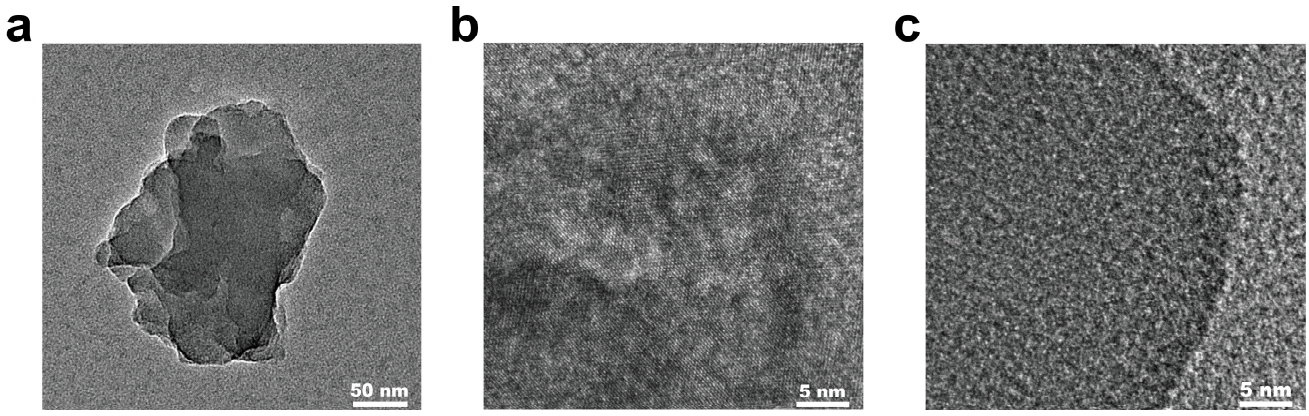



**Figure S1: HR-TEM characterization of the TpEB COF nanosheets.** (**a**) TEM image of the COF nanosheet. The nanosheets own both ordered region (**b**) and amorphous region (**c**).

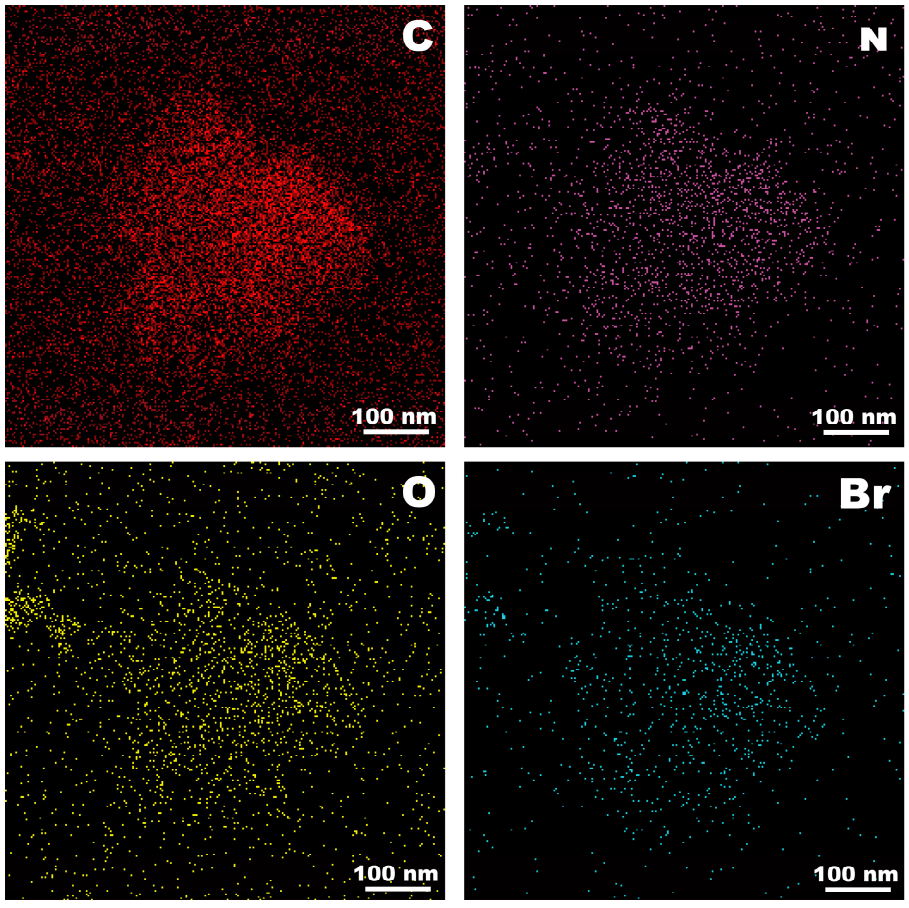



**Figure S2: TEM elemental mapping of the TpEB COF nanosheets.**

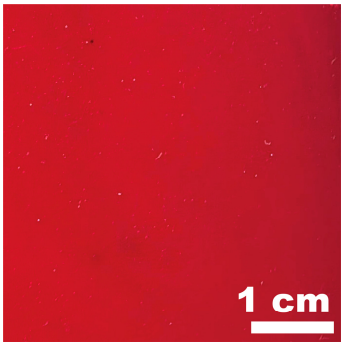



**Figure S3: Optical image of the pristine TpEB COF membrane.**

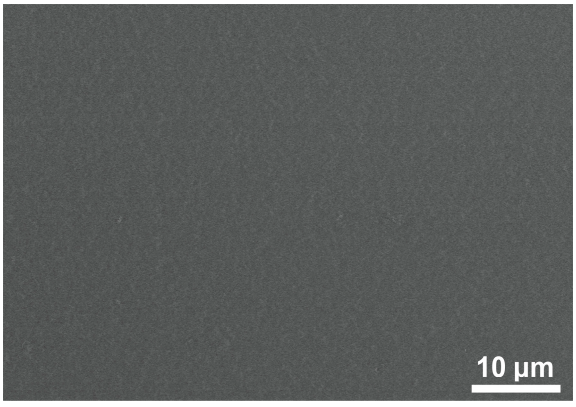



**Figure S4: Surface SEM image of the pristine TpEB COF membrane.**

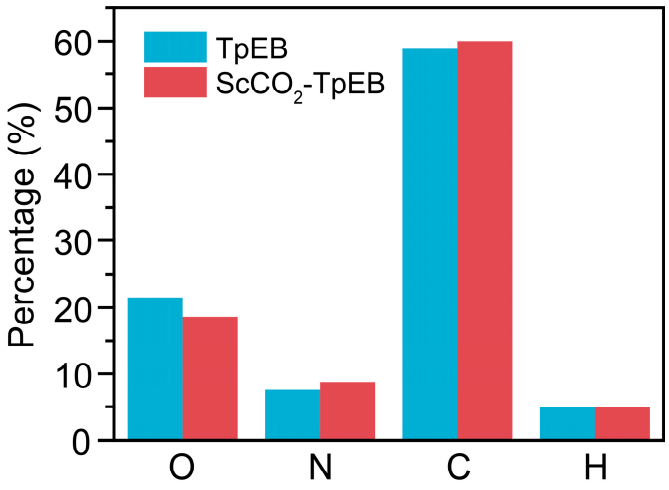



**Figure S5: EDS analysis of the element composition of the pristine and the $ScCO_2$-TpEB COF membranes.**

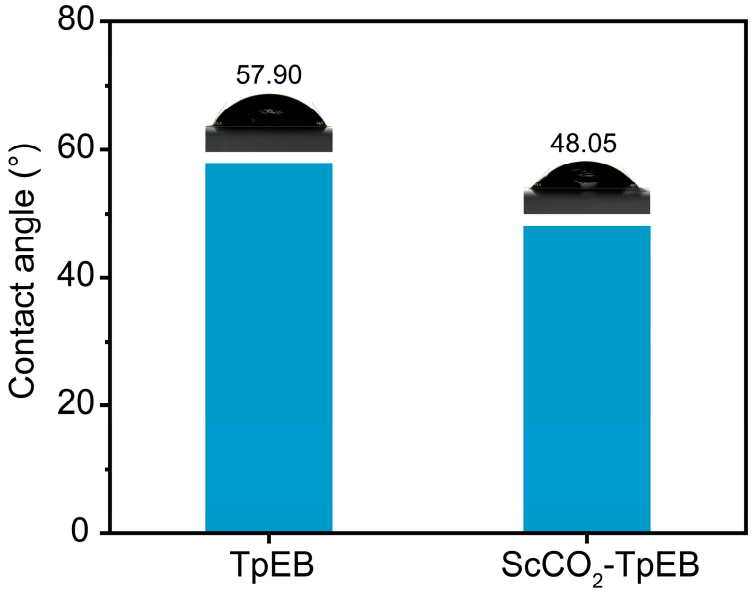



**Figure S6: Contact angle measurements of the pristine and the $ScCO_2$-TpEB COF membranes.**

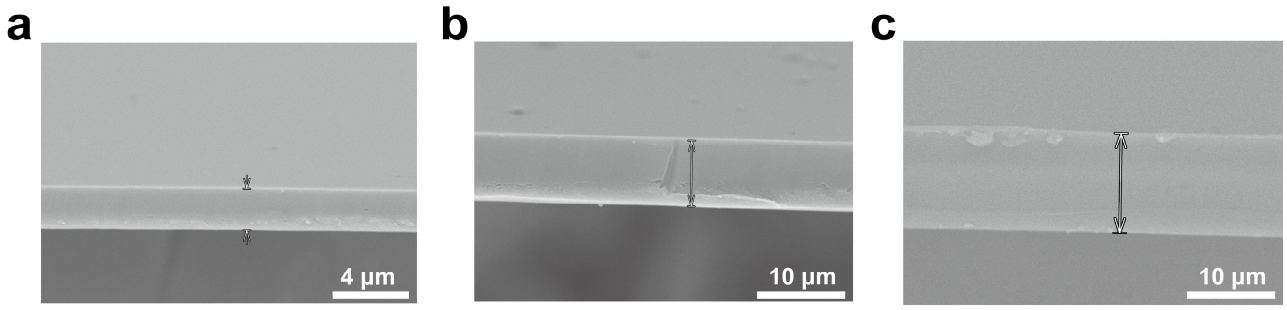



**Figure S7: Cross-sectional SEM images of the $ScCO_2$-COF membranes with varying thickness.** The thickness was (**a**) 2 μm, (**b**) 7 μm, and (**c**) 11 μm, respectively.

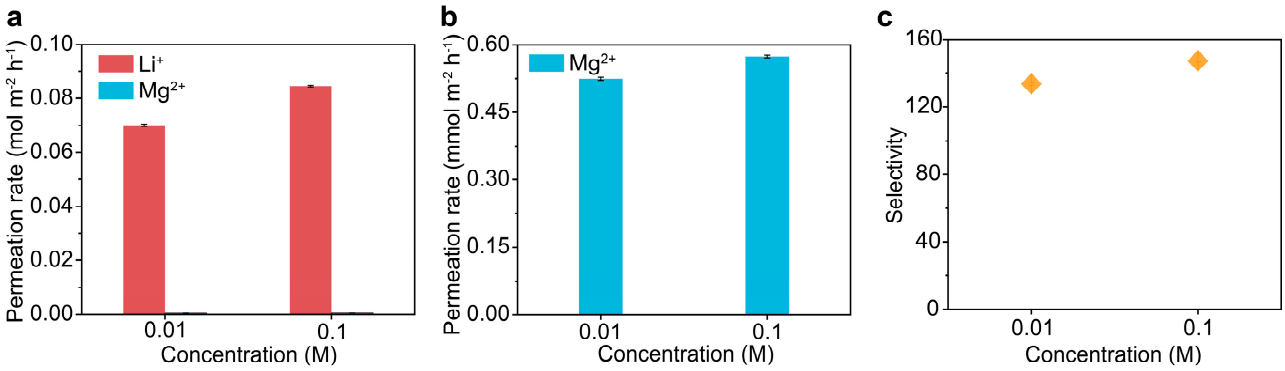



**Figure S8: Influence of feed concentration on the selective $Li^+$ transport of the $ScCO_2$ COF membrane.** (**a-b**) The influence of feed solution concentration on the $Li^+$ and $Mg^{2+}$ permeation rates. (**b**) represents the results of $Mg^{2+}$ in (a). (**c**) The influence of feed solution concentration on the $Li^+/Mg^{2+}$ selectivity.

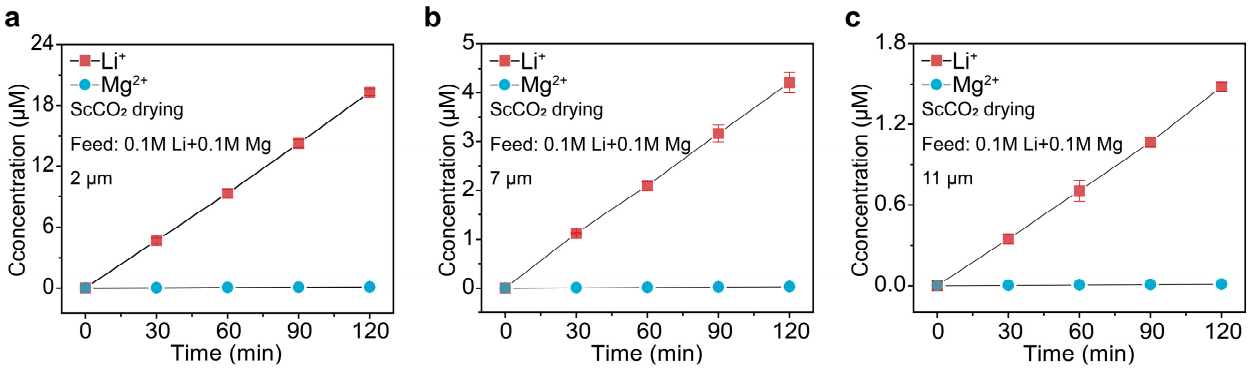



**Figure S9: Influence of membrane thickness on the selective $Li^+$ transport of the $ScCO_2$-COF membranes. (a-c)** The concentration of $Li^+$ and $Mg^{2+}$ in the permeate as a function of time for the membrane with a thickness of (**a**) 2 μm, (**b**) 7 μm, and (**c**) 11 μm, respectively.

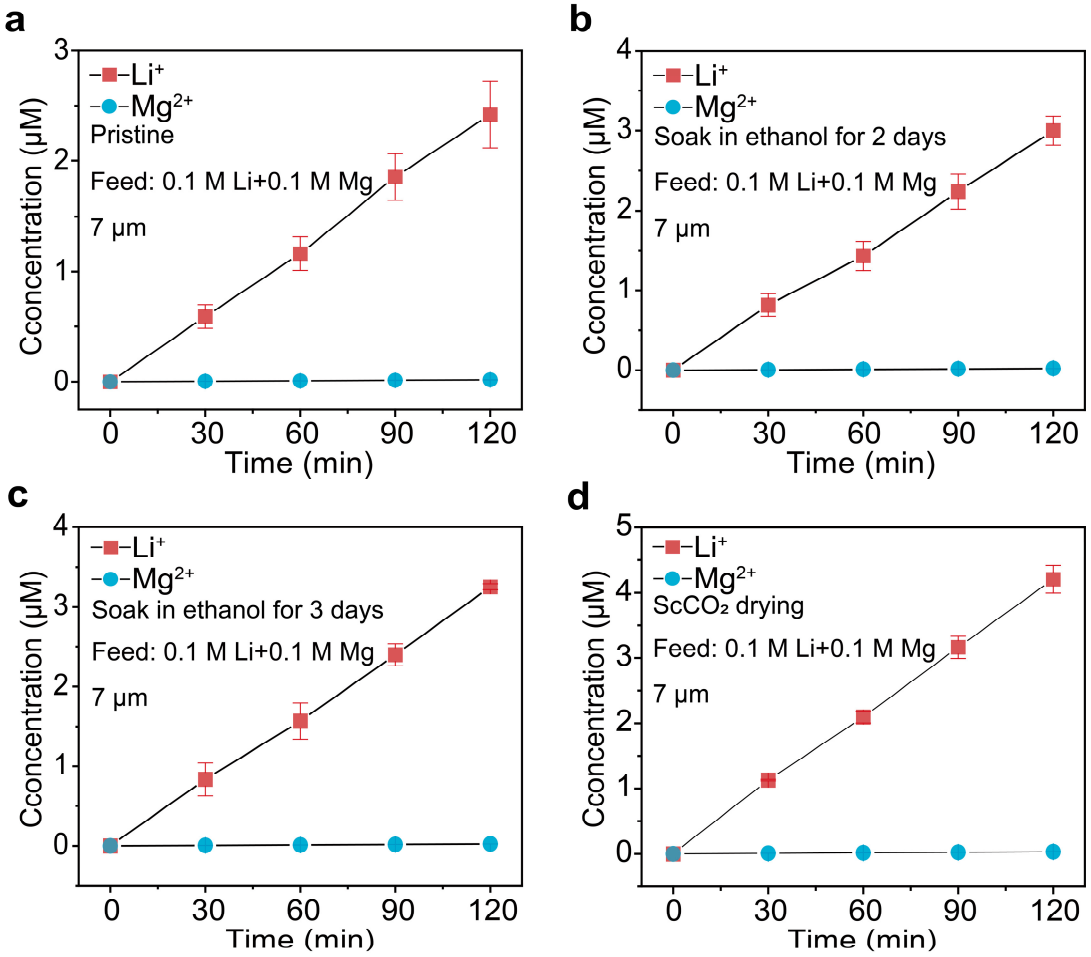



**Figure S10: The influence of $ScCO_2$ drying on the selective $Li^+$ transport of the COF membrane with a 7 μm thickness.** (**a-d**) Concentrations of $Li^+$ and $Mg^{2+}$ in the permeate along with time, for the pristine TpEB COF membrane (a), the membrane soaked in ethanol for 2 (b) and 3 (c) days before $ScCO_2$ drying, and the membrane after $ScCO_2$ drying (d).

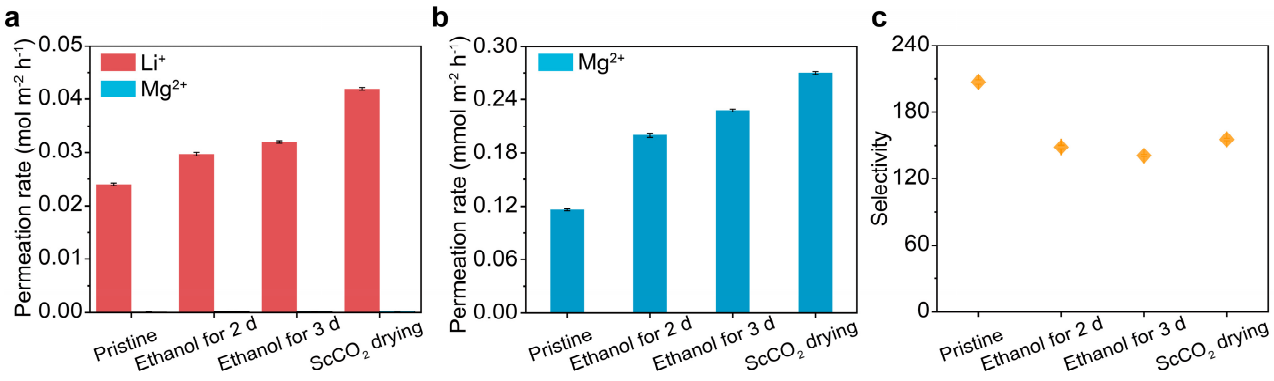



**Figure S11: The influence of $ScCO_2$ drying on the selective $Li^+$ transport of the COF membrane with a 7 µm thickness** (**a**) Comparison of the permeation rates of $Li^+$ and $Mg^{2+}$, for the pristine, ethanol-soaked, and $ScCO_2$ treated COF membranes. (**b**) The enlarge diagram, showing the permeation rates of $Mg^{2+}$ corresponding to those in (a). (**c**) The corresponding $Li^+/Mg^{2+}$ selectivity concluded from (a-b).

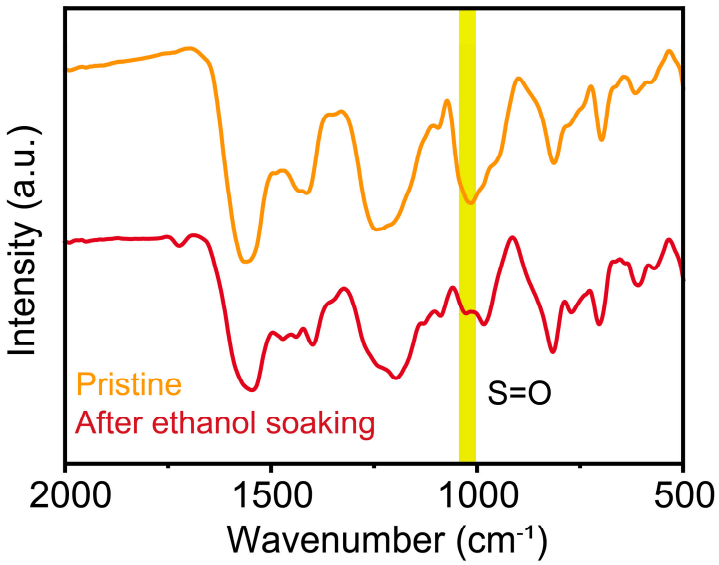



**Figure S12: FT-IR spectra of the pristine TpEB COF membrane (yellow curve) and the TpEB COF membrane after ethanol soaking (red curve).** The attenuation of the S=O stretching vibration at ~1025 $cm^{-1}$ after ethanol soaking indicates the effective removal of residual DMSO from the membrane.

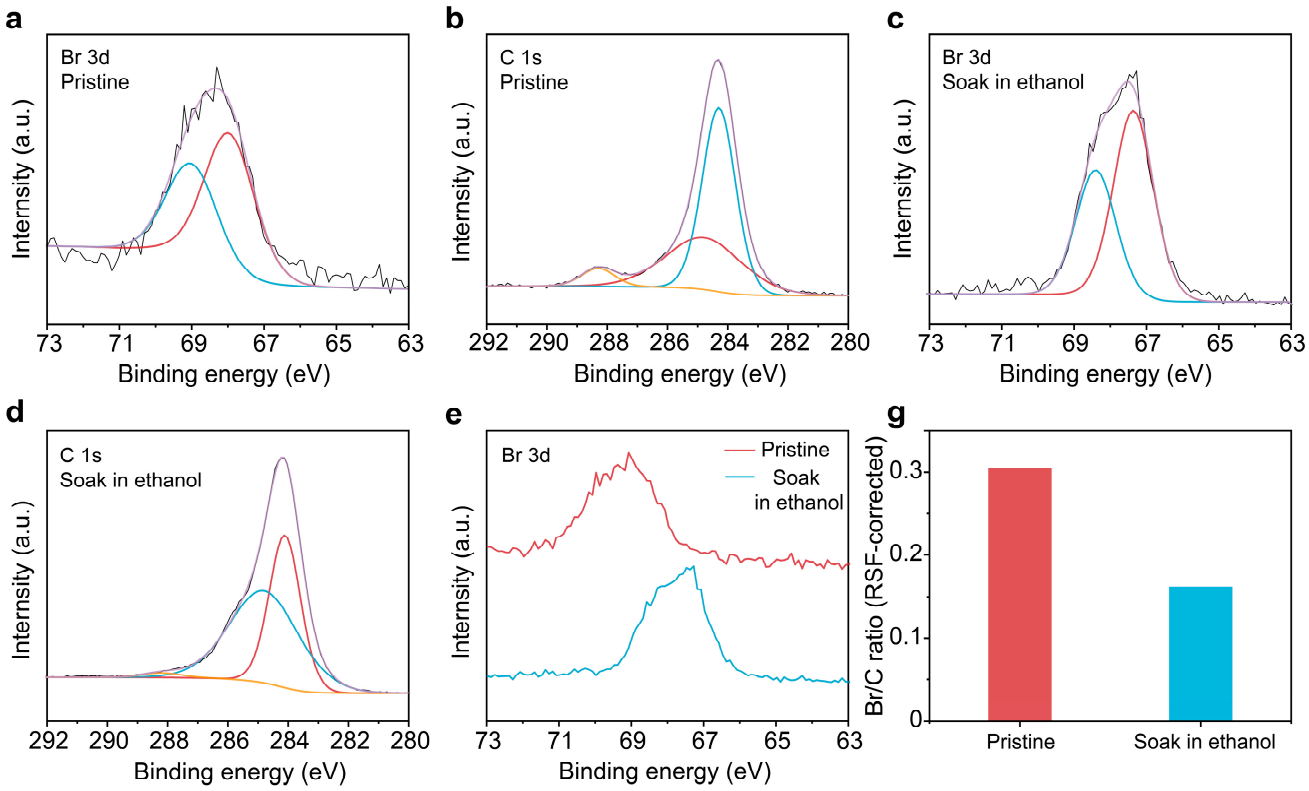



**Figure S13: XPS analysis of TpEB COF membranes before and after ethanol soaking.** (a) High-resolution Br 3d spectrum of the pristine membrane with curve fitting. (b) High-resolution C 1s spectrum of the pristine membrane with curve fitting. (c) High-resolution Br 3d spectrum of the ethanol-soaked membrane with curve fitting. (d) High-resolution C 1s spectrum of the ethanol-soaked membrane with curve fitting. (e) Comparison of Br 3d spectra for pristine and ethanol-soaked membranes (spectra vertically offset for clarity). (g) RSF-corrected Br/C ratios derived from background-subtracted integrated peak areas. The ethanol treatment results in a significant decrease in surface Br content.

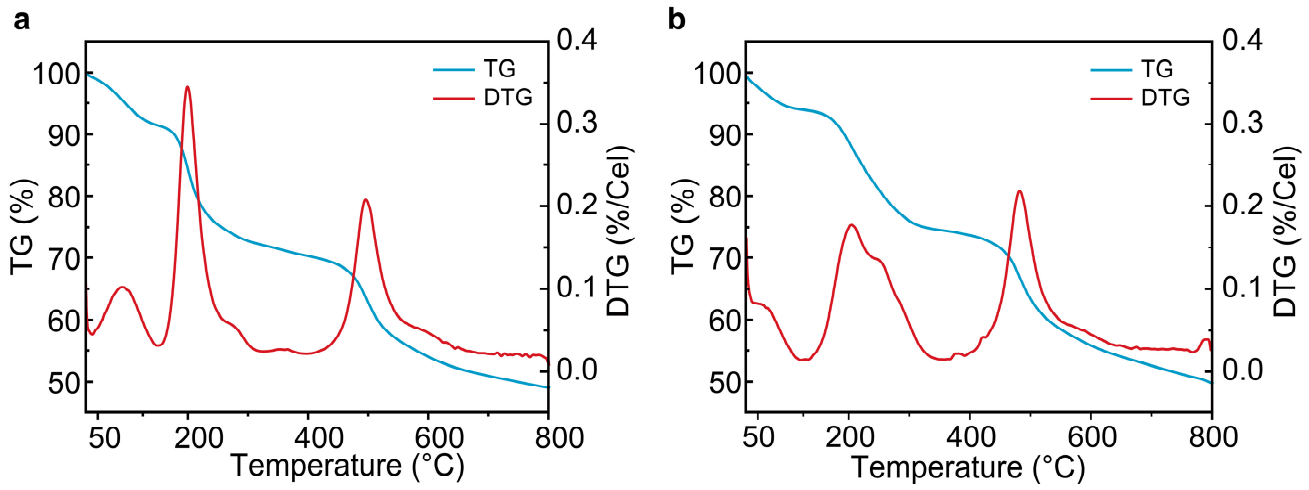



**Figure S14: TGA analysis of the pristine TpEB COF membrane (a) and the TpEB COF membrane subjected to ethanol soaking followed by $ScCO_2$ drying (b).** The markedly reduced weight loss in the low-temperature region (120–250 °C) after the treatment indicates the effective removal of residual DMSO and weakly bound monomers trapped within the membrane.

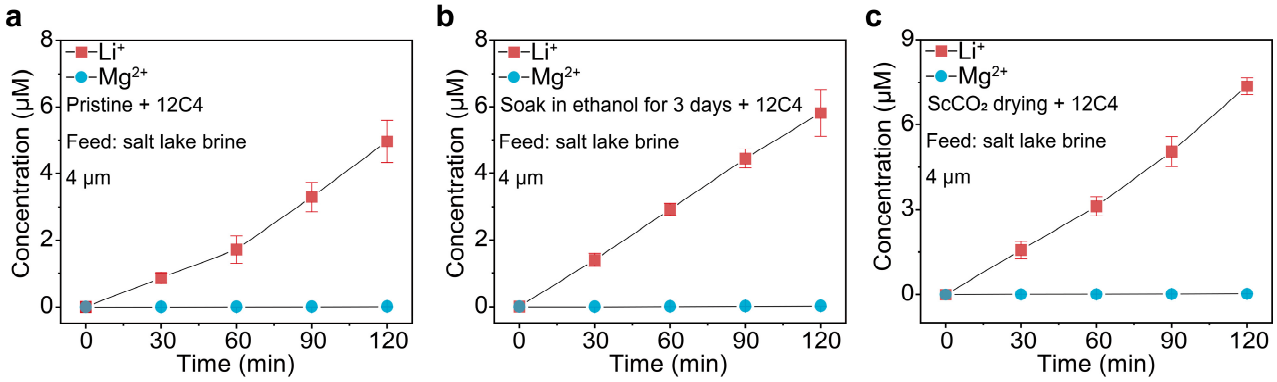



**Figure S15: The influence of $ScCO_2$ drying on the selective $Li^+$ transport of the COF membrane doped with 12C4 crown ether. (a-c)** Concentrations of $Li^+$ and $Mg^{2+}$ in the permeate along with time, for the pristine membrane (a), the one soaked in ethanol for 3 (b) days before $ScCO_2$ drying, and the membrane after $ScCO_2$ drying (c).

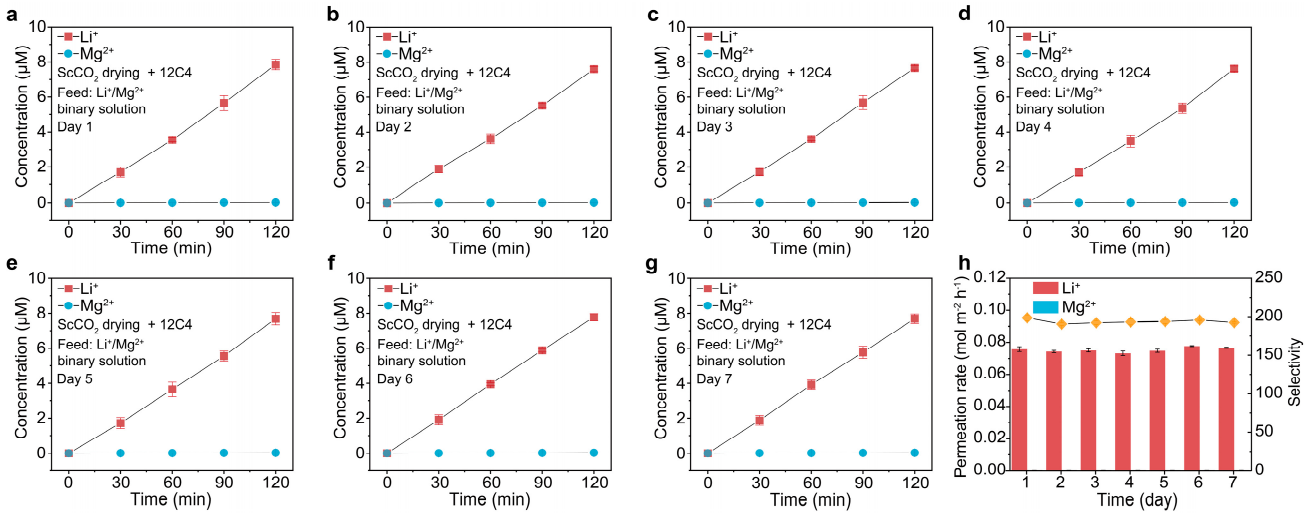



**Figure S16: Long-term $Li^+$ separation performance of the crown ether-functionalized $ScCO_2$-COF membrane using $Li^+/Mg^{2+}$ binary solution as the feed. (a-g)** Concentrations of $Li^+$ and $Mg^{2+}$ in the permeate as a function of time. (**h**) Comparison of the permeation rates of $Li^+$ and $Mg^{2+}$ and the corresponding $Li^+/Mg^{2+}$ selectivity.

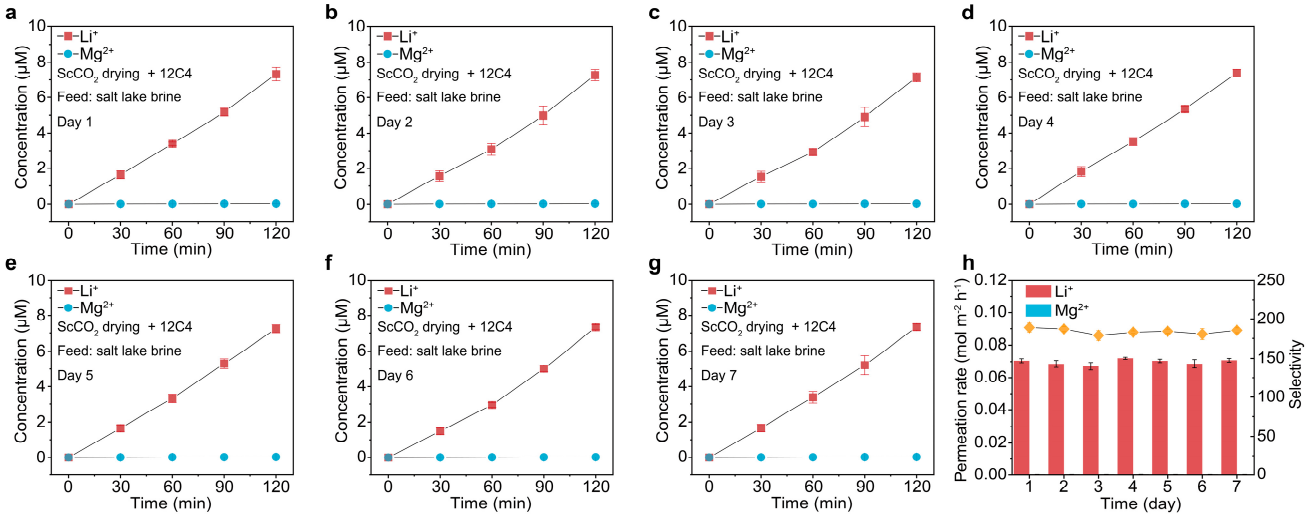



**Figure S17: Long-term $Li^+$ separation performance of the crown ether-functionalized $ScCO_2$-COF membrane using real salt lake brine as the feed. (a-g)** Concentrations of $Li^+$ and $Mg^{2+}$ in the permeate as a function of time. (**h**) Comparison of the permeation rates of $Li^+$ and $Mg^{2+}$ and the corresponding $Li^+/Mg^{2+}$ selectivity.

**Table S1: Ionic composition of the water from Qinghai Lake, China.**

| Ion type | $Li^+$ | $Na^+$ | $K^+$ | $Ca^{2+}$ | $Mg^{2+}$ |
|---|---|---|---|---|---|
| Concentration (M) | 0.035 | 2.17 | 0.38 | 0.2 | 0.022 |

**Table S2: Comparison of $Li^+/Mg^{2+}$ separation performance of TpEB-$ScCO_2$ and reported membranes under concentration gradient**

| Membrane Type | Feed Solution | $Li^+$ permeation rate (mol $m^{-2}$ $h^{-1}$) | $Li^+/Mg^{2+}$ selectivity | Reference |
|---|---|---|---|---|
| TpEBr | 0.2 M $Li^+$+ 0.2 M $Mg^{2+}$ | 0.05 | 41.1 | [1] |
| TpPa-$SO_3H$ | 0.1 M $Li^+$+ 0.1 M $Mg^{2+}$ | 0.0025 | 1000 | [2] |
| p-TpPa-C≡CH | 0.05 M $Li^+$+ 0.05 M $Mg^{2+}$ | 0.025 | 102.5 | [3] |
| p-ETTBPa-C≡CH | 0.05 M $Li^+$+ 0.05 M $Mg^{2+}$ | 0.08 | 51.3 | [3] |
| TpPa-$SO_3H$ | 0.1 M $Li^+$+ 0.1 M $Mg^{2+}$ | 0.121 | 174 | [4] |
| TG-1 | 0.1 M $Li^+$+ 0.1 M $Mg^{2+}$ | 0.003402 | 423 | [5] |
| $TpBDMe_2$ | 0.1 M $Li^+$+ 0.1 M $Mg^{2+}$ | 0.0383 | 36 | [6] |
| Cu-SAV | 0.25 M $Li^+$/ 0.25 M $Mg^{2+}$ | 1.02 | 34 | [7] |
| JGOM | 0.2 M $Li^+$+ 0.2 M $Mg^{2+}$ | 0.24 | 43.5 | [8] |
| MMTM-LC | 0.1 M $Li^+$+ 0.1 M $Mg^{2+}$ | 0.11 | 38.13 | [9] |
| MMTM-LC | Lop Nor brine | 0.006 | 24.88 | [9] |
| CMM | 30 mM $Li^+$+ 0.5 M $Mg^{2+}$ | 0.0059 | 62 | [10] |
| TpEB-$ScCO_2$ | 0.1 M $Li^+$+ 0.1 M $Mg^{2+}$ | 0.085 | 147 | This work |
| TpEB-$ScCO_2$+12C4 | Salt lake brine | 0.081 | 187 | This work |

**References**


1. Wang, R.; Ding, L.; Xue, J.; Wu, H.; Cai, C.; Qiao, Z.; Caro, J.; Wang, H. Engineering of covalent organic framework nanosheet membranes for fast and efficient ion sieving: Charge-Induced Cation Confined Transport. *Small Methods* **2024**, *9*, doi:10.1002/smtd.202401111.
2. Wang, G.; Shao, L.; Zhang, S. Membrane-ion interactions creating dual-nanoconfined channels for superior mixed ion separations. *Adv. Mater.* **2025**, *37*, 2414898, doi:10.1002/adma.202414898.
3. Wang, M.; Wu, Z.H.; Zhou, G.Z.; Wu, X.Q.; Li, S.; Ma, T.Y.; Ren, Y.; Hai, G.; Wang, B.; Li, D.S. Partitioning COF membrane channels into ultramicroporous and π-Electron-Rich compartments for multicomponent ion separations. *Angew. Chem. Int. Ed.* **2025**, *64*, doi:10.1002/anie.202514179.
4. Hu, X.-F.; Jiang, T.; Fan, H.; Guan, Y.-F.; Chen, J.-J.; Yu, H.-Q.; Elimelech, M. Dual-regulated covalent organic framework membranes with near-theoretical pore sizes for angstrom-scale ion separations. *Sci. Adv.* **2025**, *11*, eady3587, doi:10.1126/sciadv.ady3587.
5. Liu, C.; Li, L.; Li, L.; He, X.; Matsuyama, H. Tuning the size and ion affinity of channels within guanidinium-based covalent organic framework membranes for efficient $Li^+/Mg^{2+}$ separation. *J. Membr. Sci.* **2025**, *734*, doi:10.1016/j.memsci.2025.124433.
6. Sheng, F.; Wu, B.; Li, X.; Xu, T.; Shehzad, M.A.; Wang, X.; Ge, L.; Wang, H.; Xu, T. Efficient ion sieving in covalent organic framework membranes with Sub-2-Nanometer channels. *Adv. Mater.* **2021**, *33*, doi:10.1002/adma.202104404.
7. Zhang, L.; Huang, Z.; Chen, Y.; Li, F.; Li, G.; Zhang, F. Highly selective lithium-ion separation by regulating ion transport energy barriers of vermiculite membranes. *ACS Nano* **2025**, *20*, 1345-1356, doi:10.1021/acsnano.5c17718.
8. Wang, S.; Fang, C.; Huang, Y.; Yi, R.; Wu, M.; Wang, Y.; Li, F.; Zhu, L.; Liang, S.; Chen, L. Bio-Inspired 2D asymmetric nanochannels for high-resolution $Li^+/Mg^{2+}$ separation. *Angew. Chem. Int. Ed.* **2025**, *64*, doi:10.1002/anie.202512310.
9. Jiang, X.; Zhang, L.; Miao, Y.; Chen, L.; Liu, J.; Zhang, T.; Cheng, S.; Song, Y.; Zhao, Y. Intrinsic roles of nanosheet characteristics in two-dimensional montmorillonite membranes for efficient $Li^+/Mg^{2+}$ separation. *Water Res.* **2025**, *276*, doi:10.1016/j.watres.2025.123291.

10. Zhang, G.; Hu, G.; Li, J.; Feng, G.; Cui, Y.; Chen, Z.; Liu, Z.; Cui, Y. Design strategies for ion-sieving charge mosaic membranes toward sustainable lithium extraction. *Proc. Nat. Acad. Sci* **2025**, *122*, e2511666122, doi:10.1073/pnas.2511666122.